Solar Energy 292 (2025) 113403

Contents lists available at ScienceDirect

Solar Energy

journal homepage: www.elsevier.com/locate/solener

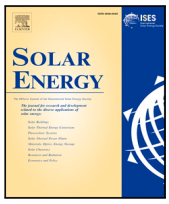

Particle mechanics and mixture homogeneity in a demonstration reactor system for the indirect reduction of redox particles

Sebastian Richter [a], Johannes Grobbel [a,*], Stefan Brendelberger [b], Martin Roeb [b], Christian Sattler [b,c]

[a] Institute of Future Fuels, German Aerospace Center (DLR), Jülich, Germany
[b] Institute of Future Fuels, German Aerospace Center (DLR), Köln, Germany
[c] RWTH Aachen, Chair of Solar Fuel Production, Aachen, Germany

ARTICLE INFO

Keywords:
Solar fuels
Thermochemical cycles
Reduction reactor
Particle mixing
DEM
Contact parameters

ABSTRACT

Many studies on two-step solar-thermochemical redox cycles for fuel production consider a combined receiver–reactor to perform the concurrent sub-processes of radiation absorption and reaction, which implies process limitations and increased technical complexity. Designed to circumvent this, an indirect concept uses an inert Al_2O_3 particle cycle absorbing heat in a receiver and transferring it to the particulate $SrFeO_{3-\delta}$ redox material in a common reactor. This Particle Mix Reactor (PMR) has been experimentally demonstrated and is investigated here in terms of particle mechanics by both measurement and simulation. With a newly developed tool for experimental particle bed segmentation, the spatial distribution of mixture homogeneity could be determined. DEM simulations – beneficial for the representation of dissimilar particle types – require mechanical contact parameters, that were obtained via an adapted systematic calibration procedure. Al_2O_3 and $SrFeO_{3-\delta}$ particles clearly differ in their results for similar collisions, especially concerning the rolling friction coefficient and the coefficient of restitution. Experimental results were reproducible, and no effect of temperature on mixture homogeneity could be identified. A significant improvement potential of mixture quality was revealed, with Al_2O_3 to $SrFeO_{3-\delta}$ particle mass ratios of about 3.5 for the upmost bed layer and of about 0.5 for the lower ones. Simulation results are satisfactorily consistent with experimental results, both qualitatively for particle motion, and for mixture homogeneity at a mean deviation of 26%. This makes the simulation model valid for further design and optimization purposes and facilitates the subsequent analysis of simulated temperature results.

1. Introduction

Technologies helping to phase out CO_2 intensive electricity generation are proven and become increasingly cost effective [1]. Certain industry sectors, however, such as aviation, iron ore direct reduction, and fertilizer production, cannot be entirely electrified and will continue to depend on liquid or gaseous fuels as dense energy carriers or reactants [2]. The massive expansion of renewable electricity generation capacity required to produce sufficient amounts of these fuels by electrolysis motivate the investigation of alternatives: Solar-thermochemical pathways are promising, especially two-step cycles using metal oxide redox materials to directly convert concentrated solar heat into chemical energy at high efficiency [3–8]. Potential products are hydrogen and carbon monoxide, oxygen and oxygen-depleted air as well as, after further conversion in downstream processes, liquid hydrocarbons and ammonia, often termed *solar fuels*. In two-step cycles, the redox material – mostly used in the shape of particles or solid monoliths – is cycled between a high-temperature reduction reaction step and a lower-temperature oxidation reaction step, in which the fuel or oxygen-depleted air is produced, see the *Redox cycle* part of Fig. 1. The approximate temperature levels for reduction and oxidation are 1400 °C and 900 °C for water splitting, and 800 °C and 400 °C for air separation, respectively.

In most of the related concepts, thermal reduction is performed in a receiver-reactor, i. e., an irradiated reactor. A number of corresponding theoretical studies showed that it may be difficult to address the different requirements limiting the reaction progress in a receiver-reactor [3,9,10]. Operational compromises arise from competing, simultaneously running sub-processes: Absorption of radiation, heat transfer into the material, the reduction reaction and the removal of oxygen. As these take place simultaneously, but on different time scales, there is no distinct optimum for material residence time [11]. Beyond this, there are

* Corresponding author.
E-mail address: johannes.grobbel@dlr.de (J. Grobbel).

https://doi.org/10.1016/j.solener.2025.113403
Received 13 December 2024; Received in revised form 7 February 2025; Accepted 4 March 2025
Available online 18 March 2025

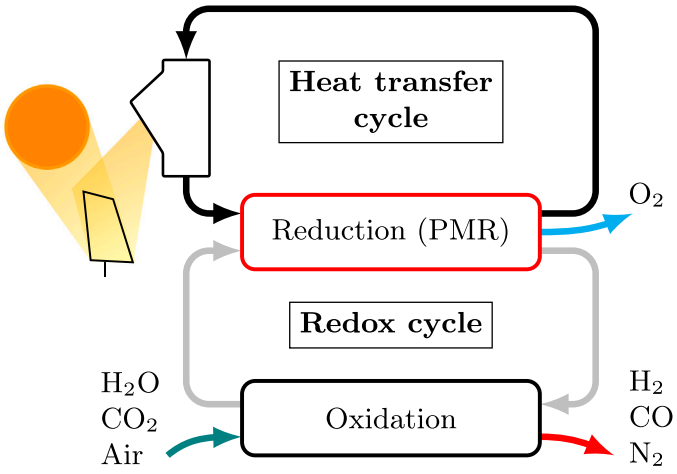

Fig. 1. Indirect redox concept scheme including the Particle Mix Reactor (PMR).

practical challenges in handling reactive materials in environments of high temperature and controlled atmosphere with incorporated concentrated radiation. Especially particle-based cycles face the generation of dust and its deposition on windows. To alleviate these limitations and to increase design and operational flexibility, an indirect particle-based redox concept was proposed by Brendelberger and Sattler: A system that, in addition to redox particles, utilizes a separate cycle of inert particles for heat transfer from a dedicated receiver to the reduction reactor, the Particle Mix Reactor (PMR) as shown in Fig. 1 [12]. Redox particles at lower temperature, coming from the oxidation reactor, and inert particles heated in the receiver are being mixed, remain in contact for heat transfer and reaction in the evacuated reactor chamber, and are mechanically separated subsequently, compare Fig. 2. In this way, solar receiver and reactor may be decoupled and individually optimized. The indirect concept thus has the potential to enhance process efficiencies compared to systems involving receiver-reactors.

For demonstration and experimental investigation of the concept and the basic functionality of the PMR, a reactor setup was designed and constructed that preheats particles to their respective temperatures and facilitates automated mixing and thermal reduction under vacuum conditions as described in [13]. It allows to record particle motion and perform measurements on mixture homogeneity, particle temperatures, heat losses, pressure, and released amounts of oxygen. Evacuation is applied to lower the oxygen partial pressure in the reactor and facilitate thermal reduction. Details on the setup, measurement techniques and the procedure are given in Section 2.2.

To simulate the process taking place in the PMR, to achieve a more detailed analysis of basic principles, and to build an assessment tool for prospective systems after modification or scale-up, we developed a detailed numerical model based on the Discrete Element Method (DEM). Compared to other particle-based redox concepts for solar fuel production, a specificity here is the presence and mechanical interaction of two different particle types. Beyond that, the model covers heat transfer, especially thermal radiation, by incorporating a program developed by Grobbel [14], and a contribution by the reduction reaction. In this paper, however, we focus on particle mechanics, i. e., particle motion during the mixing process and, as its result, the homogeneity of the binary mixture in the reactor chamber. Regarding the low effective thermal conductivity of granular media, the spatial distribution of particles in the mixture – heat transfer particles at higher temperature and redox particles at lower temperature – largely affects heat transfer between them. The higher the mixture homogeneity, the smaller the average distance between particles of different types. Thus, knowing the mixture homogeneity allows to implement improvements

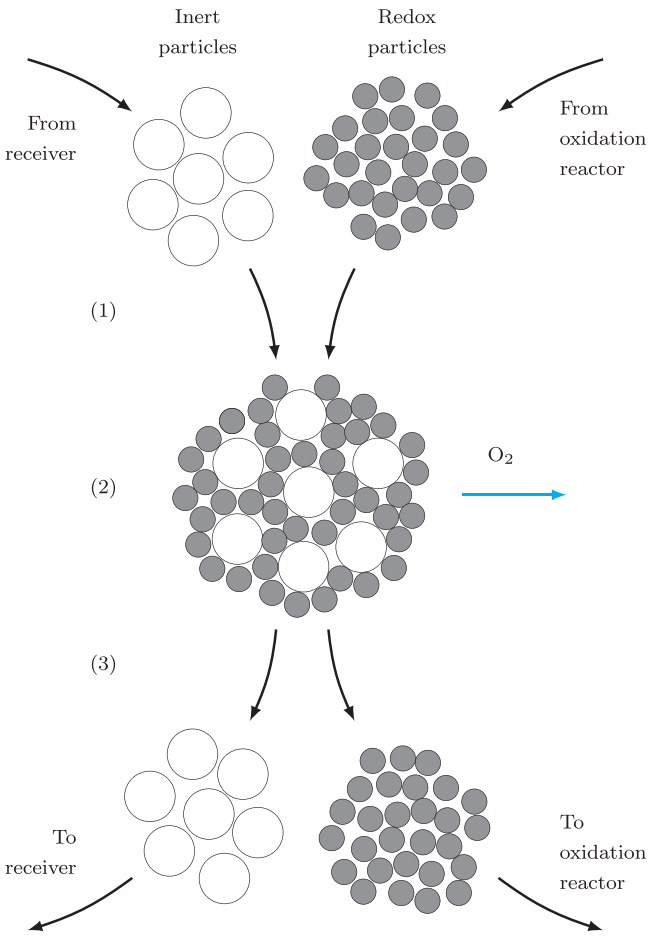

Fig. 2. Working principle of the Particle Mix Reactor: (1) Mixing of inert particles and redox particles (2) Heat transfer, reaction and oxygen removal from the mixture (3) Mechanical separation.

that lead to quick heating of redox particles and consequently a shorter reaction time period.

The accurate simulation of particle motion by DEM requires mechanical contact parameters of the involved materials to be known or to be determined. These were obtained from a calibration procedure using lab tests sensitive to different parameters as proposed in [15]. It originally considers uniform (monodisperse) particles only, and we extend it to account for interactions between nonuniform particles as described in Section 3.

For the experimental determination of mixture homogeneity, a novel tool was designed that enabled the non-destructive fragmentation of the mixture into 56 sections, for each of which the mass ratio of the two particle types was measured. Temperature dependency of the mixture homogeneity was also investigated by analyzing mixtures produced at both ambient and high temperatures. In addition to qualitative recordings of particle motion during the mixing process by a high speed camera, the measured mixture homogeneity and its spatial distribution allow a quantitative comparison of experimental and simulation results as presented in Section 4. This facilitates a validation of the numerical model in terms of particle mechanics, which is a crucial condition to be able to interpret further results of temperature distribution in the binary particle bed.

Table 1
Particle properties.

		$SrFeO_{3-\delta}$	Al_2O_3
Density ρ	$\frac{kg}{m^3}$	3460	3690
Sauter diameter $\bar{d}_{32}$	mm	1.47	2.99
Mean circularity $\bar{\Psi}$	–	0.971	0.962

2. Materials and methods

2.1. Particles and their properties

The perovskite material $SrFeO_{3-\delta}$, which can be used for air separation, was selected for experimentation due to its good reducibility at moderate temperatures [16]. Its nonstoichiometric redox characteristic is similar to that of ceria, the benchmark water splitting redox material. Ceria itself could not be tested, as the maximum available furnace temperature of 1100 °C is not sufficient to reduce it significantly. The $SrFeO_{3-\delta}$ material was synthesized and converted into 1.6 kg of particles via an in-house granulation method. Al_2O_3 milling beads (92% purity) were used as heat transfer particles. Both particle types were characterized in terms of density, particle size distribution, and circularity Ψ, that is, a measure of an object's resemblance to a circle used in 2D image analysis of randomly oriented 3D objects (with a value of unity for a perfect sphere). The Sauter diameter $\bar{d}_{32}$ corresponds to the diameter of a particle of equivalent specific surface area, and its relative measurement uncertainty was determined to be <1% here. All particles of the same type are assigned their respective value of $\bar{d}_{32}$ in the simulation. The resulting particle properties are summarized in Table 1.

2.2. Experimental setup

All heat required for thermal reduction of redox particles in the reactor chamber must be provided by heat transfer particles, as the chamber is not actively heated. The experimental setup was therefore designed to ensure minimum heat losses during the mixing process. This was achieved by a direct connection between furnace tubes and mixer, allowing a quick insertion of hot particles into the mixer, as well as by a low residence time of particles in the mixer. The setup is depicted in Fig. 3, its main components – two vertical tube furnaces, the mixing unit and the vacuum reactor chamber – are directly connected. This section describes the procedure of experimentation and the determination of mixture homogeneity. Detailed specifications of the setup are found in [13].

2.2.1. Experimental procedure

The experimental procedure and the different experimentation phases are illustrated in Fig. 3. The furnaces are manually charged with 1 kg of Al_2O_3 and 1 kg of $SrFeO_{3-\delta}$ particles, respectively, and bed temperatures are allowed to homogenize. Particles were placed in the furnaces' constant temperature zones with their locations indicated by the manufacturer. Once the temperature measured by an inserted thermocouple reaches the setpoint, the experimental run is initiated by automated release of the particle valves. The particles valves are equipped with bell-shaped plugs at their lower ends to keep particles in place. The valves fall down to their end positions, at which they are being decelerated by shock absorbers. The valve for Al_2O_3 particles opens first, while a delay of the $SrFeO_{3-\delta}$ particle release was set to 125 ms in all experiments. Due to variations in the actuators' response times and due to friction between particle valves, particles and furnace tube, the actual delay of the $SrFeO_{3-\delta}$ particle release was later found to vary between 100 ms and 130 ms in the experiment. Particles enter the mixer, run down the ramp and result in a mixture eventually guided into the reactor chamber, settling approximately 3 s after particle valve release. Mixer and reactor chamber lining were manufactured from a refractory material (Rath KVS 164/302). It was coated on the inside using an alumina cement to reinforce against abrasion.

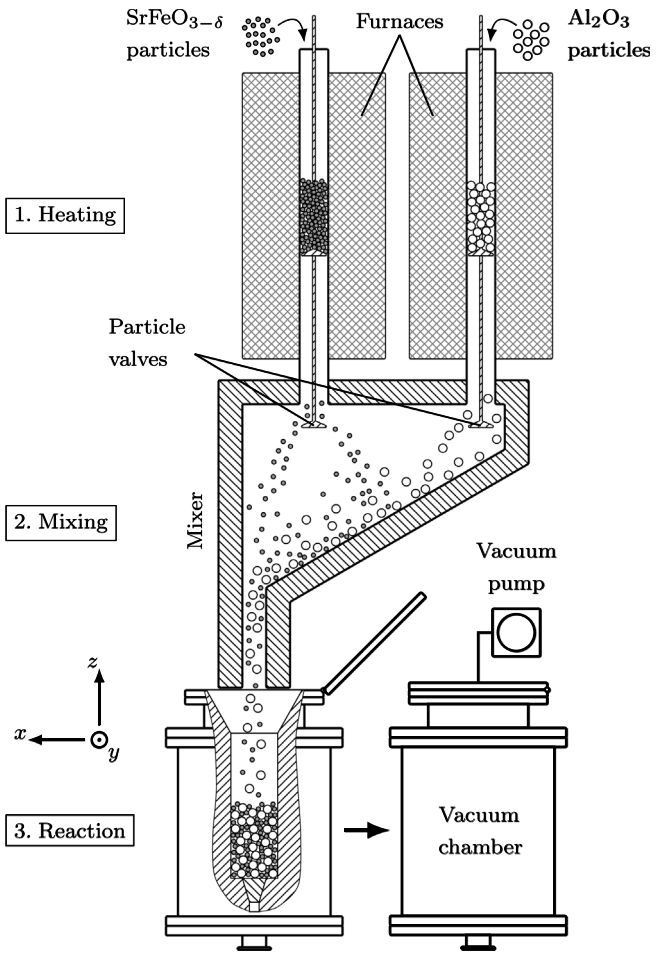

Fig. 3. Procedure of a high temperature reduction run in the Particle Mix Reactor (PMR) setup.

On an automated acoustic signal, the reactor chamber is manually shifted and the quick access door is closed. Evacuation is initiated automatically 10 s after particle valve release. Temperatures of particle bed and refractory, as well as pressure values, are logged during the evacuation period. The time required to reach the setpoint vacuum pressure of 1000 Pa depends on the amount of released oxygen and therefore on initial particle temperatures. The reactor chamber is vented after 30 minutes at maximum and the particle mixture is discharged through the bottom outlet. After having cooled down, particles are screened into different types. During each mixing process, about 1.4% of the deployed $SrFeO_{3-\delta}$ particles are attrited into fines (<0.71 mm) on average. Industrial use would thus necessitate an enhanced granulation method in terms of particle strength. Al_2O_3 particles did not show any signs of degradation. The cleared reactor chamber remains open for 12 h at minimum to cool down to ambient temperature before performing a subsequent run.

The number of experimental runs is limited through the cooling time required to restore the initial temperature as well as through particle losses by attrition. An extensive parameter study was thus out of scope in this work. Instead we focused on experimental runs to demonstrate the basic functionality of the PMR and to validate the numerical model. Initial temperatures of Al_2O_3 and $SrFeO_{3-\delta}$ particles, $T_{0,A}$ and $T_{0,S}$, were selected to be varied in the experimental plan: $(T_{0,A}, T_{0,S}) \in \{(1100\ °C, 700\ °C), (700\ °C, 400\ °C), (400\ °C, 200\ °C)\}$. These pairs were selected to allow for three levels between the onset of

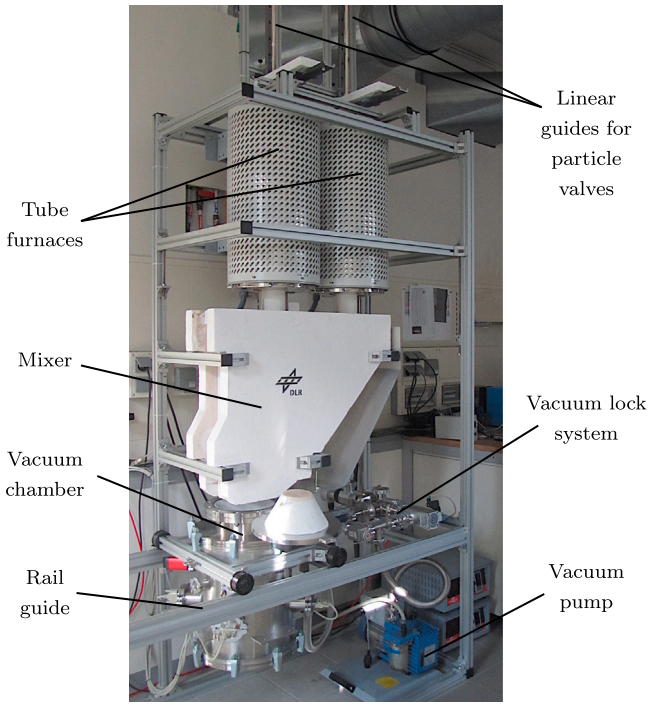

Fig. 4. Photograph of experimental setup.

thermal reduction of $SrFeO_{3-\delta}$ at approximately 300 °C and the maximum furnace temperature of 1100 °C. Other parameters like particle masses and their ratio, particle diameters and setpoint vacuum pressure were held constant. Experimental runs were repeated to obtain reliable results and to verify measurement reproducibility, except for the low temperature level as prior repeated results had been virtually identical. Fig. 4 shows a photograph of the experimental setup.

2.2.2. Mixture homogeneity

For non-destructive mixture analysis in axial and circumferential direction, a decomposition tool was developed and applied in separately conducted experiments. The tool retains particles through an intake air flow and thus allows to fragment the mixture by successively removing particle layers from a chamber without substantially modifying their structure. It was 3D printed from polylactic acid and consists of a cylindrical part that is divided into 8 sections, with a length of 2 cm and an outer diameter conforming the chamber dimension ($d = 10$ cm), see Figs. 5(a) and 5(c). Its backside is covered with a wire mesh screen to prevent particles from being entrained, as the adjoining reducing cone is connected to the suction pipe of an air fan. It is switched on after the tool has been manually pressed into the bed. Particles are lifted from the bed and guided into separate beakers by a 3D printed adapter, then screened and weighed.

Separate mixture analysis experiments are required as applying the tool in the actual reactor chamber – designed for high temperature reduction runs – is prohibited by thermocouples reaching into the particle bed. The method further requires a sufficiently high air flow into the decomposition tool and therefore a permeable chamber wall. For mixture analysis, a stainless steel wire mesh tube was thus installed replacing the reactor chamber's cylindrical refractory side wall as shown in Fig. 5(b). Differences in contact properties between refractory and wire mesh are assumed to be insignificant, as entering particles predominantly impact on the chamber bottom or particle bed surface, rather than collide with the side wall. The wire mesh's temperature resistance facilitates decomposition of mixtures from experimental runs performed at ambient as well as at high temperatures up to 1100 °C.

The structure of the segmented particle bed is shown in Fig. 6. Seven layers of particles were removed from the chamber per experimental run with eight sections each, identified by their height z above the chamber bottom and the azimuth angle φ of the section centerline. A residuum of about 1.2 cm height remained in the chamber. A quantitative analysis of uncertainty in homogeneity measurements remains pending due to its complexity; there was no practical way to calibrate the method. For a discussion of potential uncertainty contributions, see Section 4.2.2.

The mass of a particle layer retained in the tool differs per sampling (about ±10% around the mean) due to variations in local particle composition and thus air flow and drag forces. Accordingly, the simulated bed was not evaluated with an equidistant layer spacing either. The layer thickness values were adjusted to match the mean measured particle layer masses, see Table A.4. Evaluation was performed by processing the simulation result files in Python and assigning every particle to a respective section according to its position. On average, a section contains 315 Al_2O_3 particles and 2766 $SrFeO_{3-\delta}$ particles. Experimental and simulation results are presented and discussed in Section 4.2.

2.3. DEM models

There is no comprehensive theory describing the behavior of granular media especially for the combination of mechanical and thermal phenomena, hence, numerical simulation is important for apprehension and prediction. Among a number of approaches to deal with particle motion and heat transfer simultaneously, the Discrete Element Method (DEM) holds advantages in accuracy of particle dynamics. By considering the discrete nature of particles and their individual contacts, it also forms a basis suitable for heat transfer modeling. The method's fundamentals and the applied contact models are briefly summarized in the following.

2.3.1. Kinematics and dynamics

The DEM traces every particle in the simulation domain by integrating the Newtonian equation of motion [17]:

$$\frac{\mathrm{d}^2\vec{s}_i}{\mathrm{d}t^2} = \frac{1}{m_i}\sum_{c=1}^{N_c}\vec{F}_{c\to i} + \vec{g} \tag{1}$$

Here, $\vec{s}_i$ denotes the particle's position vector, m_i its mass and $\vec{F}_{c\to i}$ the force vector of (particle or wall) contact c to the particle. The contact force vectors are summed over the number of contacts N_c. Further, the particle is subject to gravitation $\vec{g}$.

Particles are assumed to be spherical and a contact between two particles i and j is considered established if the distance between their centers is smaller than the sum of their radii [18]. If this is the case, the small particle overlap generates compressive forces through elastic restitution. Other forces, such as drag, capillary, magnetic or electrostatic forces, are neglected here.

Rotational particle motion $\vec{\omega}_i$ is described analogously to Eq. (1),

$$\frac{\mathrm{d}\vec{\omega}_i}{\mathrm{d}t} = \frac{1}{I_i}\sum_{c=1}^{N_c}\vec{r}_{0,c}\times\vec{F}_{c\to i,\mathrm{t}} + \frac{1}{I_i}\vec{M}_{\mathrm{rf}} \tag{2}$$

with relevant contributions by the tangential contact force component $\vec{F}_{c\to i,\mathrm{t}}$ and a rolling friction torque $\vec{M}_{\mathrm{rf}}$ to account for deviations from the assumption of ideal spherical particles [18]. The vector $\vec{r}_{0,c}$ faces from the particle center to the contact point and the moment of inertia becomes $I_i = \frac{2}{5}m_i R_i^2$ (R_i: particle radius), as the particle is regarded to be of homogeneous density.

Particle velocities and positions are calculated using a leapfrog algorithm using the integration time step Δt, that needs to be sufficiently small to assure a stable simulation. A corresponding critical time step Δt_c can be calculated depending on the ratio of a particle radius to the speed of a Rayleigh wave [17]. A common measure to reduce

(a) Empty tool (b) Wire mesh chamber (c) Particles in the tool

Fig. 5. Decomposition tool for experimental analysis of particle mixture homogeneity.

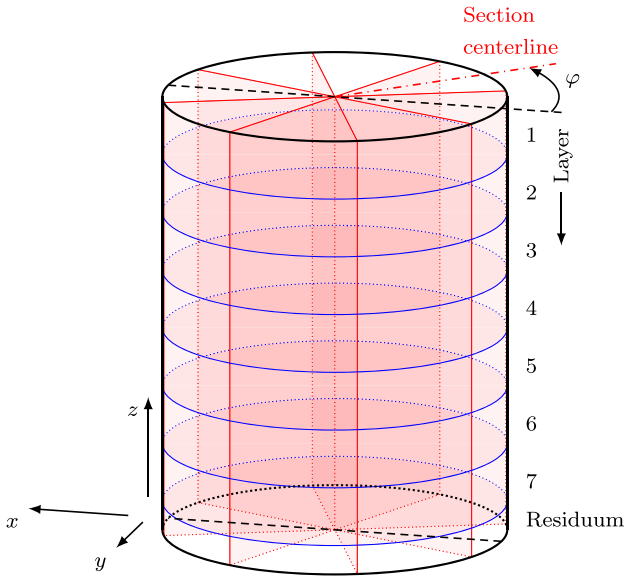

Fig. 6. Segmentation structure for analysis of mixture homogeneity in the simulated particle bed.

computational cost is to decrease the shear modulus $\overline{G}$ to allow for a larger time step [19,20]. Here, the Young's modulus was chosen to $\overline{Y} = 5\,\text{MPa}$ at a Poisson's ratio of $\nu = 0.3$, resulting in a shear modulus of $\overline{G} = 1.92\,\text{MPa}$. Deviations from actual physical properties can be compensated for by calibration of contact parameters (Section 3). A time step of $\Delta t = 2 \cdot 10^{-5}\,\text{s}$, which corresponds to $0.189\Delta t_c$, was used for the simulation phase involving particle motion, i. e., the mixing process. The open-source DEM software LIGGGHTS® was applied.

2.3.2. Contact forces and torques

Particle interfaces are represented by a spring and a dashpot for both the normal and the tangential force components [21]. The normal force vector is given as a function of the normal particle overlap $\tilde{\delta}_n$ and the relative normal velocity of the contact partners $v_{n,rel}$ by

$$\vec{F}_{c\to i,n} = \left(\underbrace{\tilde{k}_n \tilde{\delta}_n}_{\text{Spring component}} - \underbrace{c_n v_{n,rel}}_{\text{Dashpot component}} \right) \vec{e}_n \,. \tag{3}$$

and therefore depends on the normal spring stiffness $\tilde{k}_n$ and the normal damping coefficient c_n, while $\vec{e}_n$ denotes the unit vector in normal direction.

Linear force models in which $\tilde{k}_n$ and c_n are independent of the overlap $\tilde{\delta}_n$ exhibit a weaker agreement to experimental results than nonlinear models [18]. The collision time between particles for instance is less well represented [22], which is a potential drawback for the accurate simulation of heat transfer phenomena [14]. The nonlinear viscoelastic Hertz contact model available in LIGGGHTS® is hence applied [23]. It describes the normal spring stiffness based on Hertzian theory for the elastic contact of two spheres [24,25], and is explicated in Appendix A.1.1.

With the unit vector in tangential direction $\vec{e}_t$, the tangential force vector is expressed analogously to Eq. (3) [26],

$$\vec{F}_{c\to i,t} = \left(\underbrace{\tilde{k}_t \tilde{\delta}_t}_{\text{Spring component}} - \underbrace{c_t v_{t,rel}}_{\text{Dashpot component}} \right) \vec{e}_t \,. \tag{4}$$

For the calculation of the tangential displacement $\tilde{\delta}_t$, see also Appendix A.1.1. Coulomb friction is incorporated through a threshold value for the tangential force vector. Its absolute value is limited to the Coulomb friction force,

$$|\vec{F}_{c\to i,t}| \le \mu |\vec{F}_{c\to i,n}| \,, \tag{5}$$

where μ is the static friction coefficient.

The resistance against rotation of real-world particles due to shape irregularities and surface roughness is included in the DEM model by adding the rolling friction drag torque $\vec{M}_{rf}$ in Eq. (2) [21]. The *modified elastic-plastic spring-dashpot model* (EPSD2) from [27] and available in LIGGGHTS® was used as it represents particle heaps well and yields consistent angles of repose, see Appendix A.1.2 for details. The rolling friction coefficient μ_r serves the limitation of the rolling friction torque analogously to Eq. (5):

$$|\vec{M}_{rf}| \le \mu_r R_{red} |\vec{F}_{c\to i,n}| \tag{6}$$

The reduced radius R_{red} is given in Eq. (A.2).

In summary, the following assumptions and simplifications were made in the model: The gas phase was neglected, particles are assumed to be of spherical shape, both particle type collectives are considered of uniform size, respectively, and shear modulus $\overline{G}$ was reduced by defining the Young's modulus $\overline{Y}$ and the Poisson's ratio ν in Section 2.3.1. The remaining required parameters are the coefficients of static friction μ, of rolling friction μ_r, and of restitution e — each for every occurring material combination. As for many real-world materials and morphologies these parameters are not available from literature, they have to be determined by the aid of experiments as specified in the subsequent section.

3. Contact parameter determination

3.1. Approach

A direct measurement of particle contact parameters involves several disadvantages [28]. It is often difficult to find and measure physical representations of the contact properties. For reasons of practical implementation, in some cases other geometries of the contact partners than applied in the actual case have to be used, e. g., coarser particles or plates. Further, for small and irregularly shaped particles especially,

a large number of samples is required to obtain a sufficient data basis that represents the assembly. In this work instead, bulk experiments were performed and represented by DEM models that are being *calibrated*, i. e., the contact *parameters* (versus *properties*) are tuned to match the experimental result [21]. This leads to the consideration of bulk effects and quantities not directly measurable, such as the rolling friction coefficient μ_r. With this method, the obtained parameters in DEM simulations do not necessarily conform physical properties. A corresponding procedure was developed by Grobbel et al. in [15] to determine contact parameters of sintered bauxite particles for the simulation of solar particle receivers. It deploys a DEM calibration framework based on *Design of Experiments* [29]. Using a latin hypercube sampling algorithm, it creates near-random set of sample points in the parameter space, interpolates the results by Kriging functions and thus provides a systematic optimization approach. Its relevant aspects are briefly reflected in the following.

For calibration of the coefficients of friction μ_{pp} (particle-particle contacts) and μ_{pw} (particle-wall contacts), the coefficients of rolling friction $\mu_{r,pp}$ and $\mu_{r,pw}$ as well as the coefficients of restitution e_{pp} and e_{pw}, a series of experiments was used and represented by DEM simulations. In sensitivity studies, the respective experiments were found to be sensitive to different input parameters. The *angle of repose* test is significantly sensitive to the coefficients of sliding friction and rolling friction, both for particle-particle (μ_{pp} and $\mu_{r,pp}$) and particle-wall (μ_{pw} and $\mu_{r,pw}$) contacts. To increase the test's selectivity for parameters, a single layer of particles is adhered onto the base plate, which eliminates the dependency of the angle of repose β on μ_{pw} and $\mu_{r,pw}$. In the *horizontal conveyor* test, particles are conveyed via a horizontal chute with the relevant quantity being the fill time t_{30} needed until 30 g of particles have reached a bin placed on a balance at the discharge end. Again, this test is sensitive to all four sliding friction and rolling friction coefficients and was made independent of particle-wall parameters by adhering a single layer of particles onto the oscillating conveyor surface. To account for particle restitution, the *impact plate* test was designed in which particles are falling from a hopper through a tube onto a plate tilted at 45° that directs them towards four bins placed in different distances to the plate. Output quantities are the masses in the respective bins m_1, m_2, m_3, and m_4, where the indices are ascending with the distance between bin and plate. The sensitivity study revealed that all four masses depend on the particle-wall restitution coefficient e_{pw} and only m_1 depends on e_{pp}. With known sliding friction and rolling friction coefficients, the masses m_1, m_2, and m_3 from this experiment suffice for the determination of e_{pp} and e_{pw}.

Using these dependencies, six unknown parameters were determined over three stages in [15]. In the first stage, particle-particle sliding friction and rolling friction coefficients, μ_{pp} and $\mu_{r,pp}$, are determined. This is achieved by adjusting their values so that the angle of repose test as well as the horizontal conveyor test (both using adhered particle layers) yield simulation results that match those from experiments. With μ_{pp} and $\mu_{r,pp}$ known from the first stage, the second stage serves to determine the particle-wall sliding friction and rolling friction coefficients μ_{pw} and $\mu_{r,pw}$. Again, the angle of repose and the horizontal conveyor test are employed, while fixed layers of particles are removed to introduce particle-wall interactions. The third stage yields the coefficients of restitution e_{pp} and e_{pw}, with only m_1 being sensitive to e_{pp} and the masses m_2 and m_3 showing peaks at different values for e_{pw}. The procedure is illustrated in the upper section of Fig. 7 and was extended in this work as described subsequently.

3.2. Implementation and extension

The approach by Grobbel et al. delivers parameters for contacts between uniform particles, i. e., similar collisions, and parameters between each particle type and walls [15]. With the subscripts A for Al_2O_3 and S for $SrFeO_{3-\delta}$, the present correspondents are

- the coefficients of sliding friction between same-type particles, μ_A and μ_S,
- the coefficients of sliding friction between particles and walls, μ_{Aw} and μ_{Sw},
- the coefficients of rolling friction between same-type particles, $\mu_{r,A}$ and $\mu_{r,S}$,
- the coefficients of rolling friction between particles and walls, $\mu_{r,Aw}$ and $\mu_{r,Sw}$,
- the coefficients of restitution between same-type particles, e_A and e_S, and
- the coefficients of restitution between particles and walls, e_{Aw} and e_{Sw}.

Newly developed in this work is an extended procedure for dissimilar particles. The additional composite parameters between Al_2O_3 and $SrFeO_{3-\delta}$ particles are

- the composite coefficient of sliding friction μ_{AS},
- the composite coefficient of rolling friction $\mu_{r,AS}$, and
- the composite coefficient of restitution e_{AS}.

The approach for the determination of these composite parameters is described in the following.

3.2.1. Composite coefficients of friction and rolling friction

For determination of μ_{AS} and $\mu_{r,AS}$, a fourth stage was appended to the calibration procedure. The angle of repose and the horizontal conveyor test were adopted, except that the fixed particle layers consist of the one particle type and the mobile particles of the other. In this way, composite particle interaction is facilitated at the top surface of fixed particles. In practice, the coarse Al_2O_3 particles were used on an adhered layer of finer $SrFeO_{3-\delta}$ particles, as the reverse order lead to interstices between coarse particles filled up with finer particles and thus limited interaction. The calibration procedure is similar to the first stage, see Section 3.3 for results. All lab tests were conducted at ambient temperature. A discussion of the effect of temperature on contact parameters is found in Section 4.2.

A calibration approach was considered unsuitable for the composite restitution coefficient e_{AS}. First, this would imply an extensive DEM sensitivity study. Second, an exact particle mixture homogeneity required for this approach is difficult to be reproduced in a test setup. Therefore, e_{AS} is analytically derived from the calibrated restitution coefficients for similar particles, which is described in the subsequent section. Its value is used in the fourth stage for calibration of μ_{AS} and $\mu_{r,AS}$, so that a study of the dependency of β and t_{30} on e_{AS} in the composite angle of repose and horizontal conveyor experimental runs becomes obsolete. Fig. 7 summarizes the entire contact parameter determination procedure including the introduced extensions.

3.2.2. Composite coefficient of restitution

Coaplen et al. present a general equation for the prediction of a composite coefficient of restitution of nonconforming collision partners of different materials when the coefficients of restitution for similar collisions are known [30]. It is based on an energetically consistent description of the impact. The composite coefficient of restitution e_{AS} between Al_2O_3 and $SrFeO_{3-\delta}$ particles is accordingly given by

$$e_{AS}^2 = \frac{e_A^2 W_A + e_S^2 W_S}{W_A + W_S} = \frac{e_A^2 \int_0^{\tilde{\delta}_{n,max,A}} F_n \mathrm{d}\tilde{\delta}_A + e_S^2 \int_0^{\tilde{\delta}_{n,max,S}} F_n \mathrm{d}\tilde{\delta}_S}{\int_0^{\tilde{\delta}_{n,max,A}} F_n \mathrm{d}\tilde{\delta}_A + \int_0^{\tilde{\delta}_{n,max,S}} F_n \mathrm{d}\tilde{\delta}_S}, \tag{7}$$

with W_A and W_S as the energy stored in the Al_2O_3 and the $SrFeO_{3-\delta}$ particle, respectively, at the end of the compression phase. For their calculation, the compressive normal force F_n is integrated over the deflections $\tilde{\delta}_A$ or $\tilde{\delta}_S$, where $\tilde{\delta}_{n,max,A}$ and $\tilde{\delta}_{n,max,S}$ correspond to maximum compression. A simplification is used at this point: The contact model in Section 2.3.2 in fact contains a dashpot component. A consideration

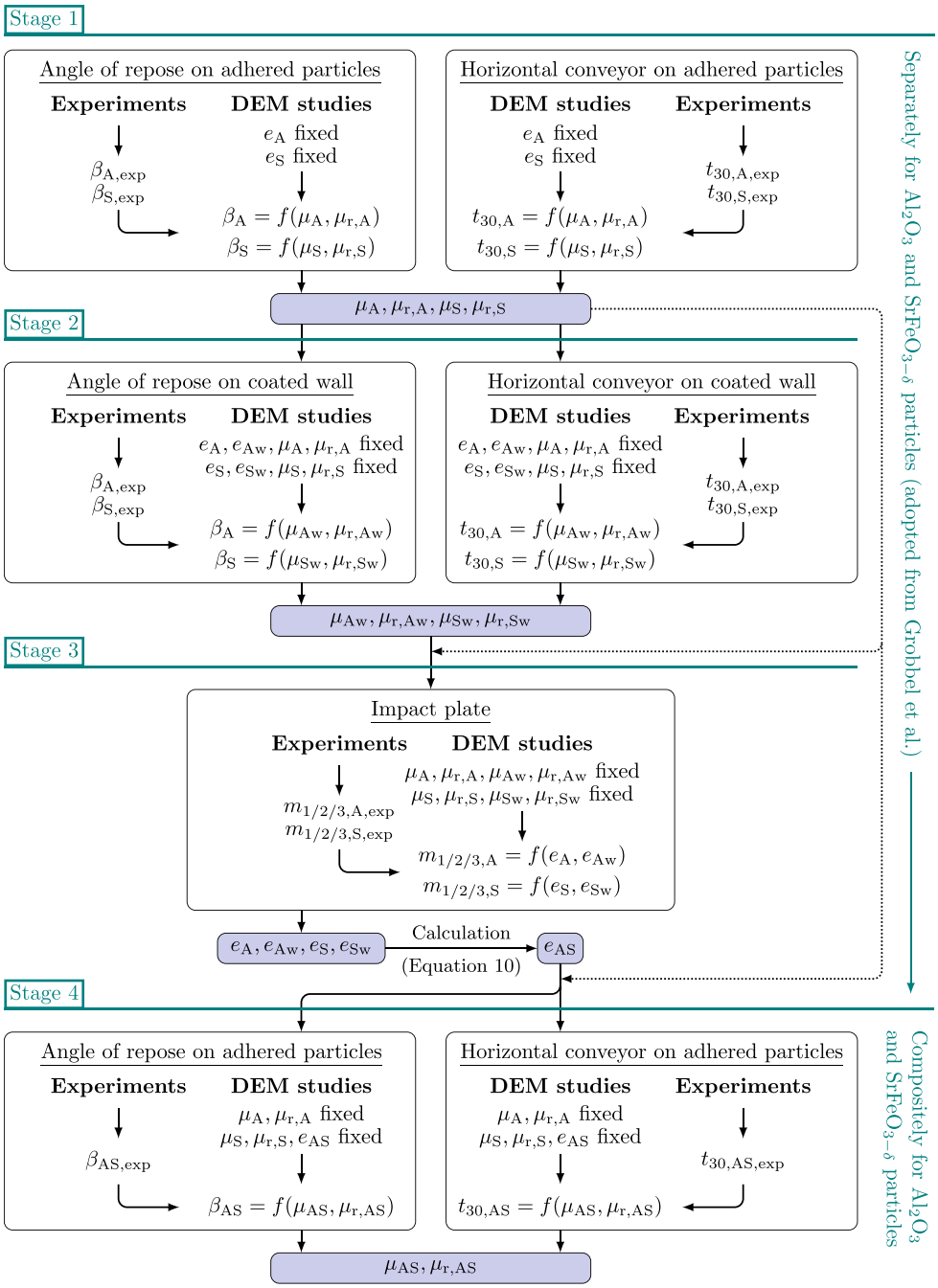

Fig. 7. Contact determination procedure. First three stages were adopted from [14], the fourth stage appended for parameters between nonuniform particles. The composite coefficient of restitution e_{AS} was derived analytically.

of its velocity dependency, however, would require a detailed analysis of relative impact velocities present in the PMR. As an effect of velocity is included in the previously calibrated values of e_A and e_S, the normal force F_n is approximated by the rate-independent law, i. e., expressed only by the spring component from Eq. (3), which is in accordance to Coaplen et al. [30]. The normal spring stiffness $\tilde{k}_n$ is given in Eq. (A.1) and depends on the reduced radius R_{red} and the reduced Young's modulus $\bar{Y}_{red}$. For similar collisions, that is, $R_i = R_j = R$ and $\bar{Y}_i = \bar{Y}_j = \bar{Y}$, these are $R_{red} = \frac{R}{2}$ according to Eq. (A.2) and $\bar{Y}_{red} = \frac{\bar{Y}}{2(1-\nu^2)}$ according to Eq. (A.3). The corresponding compression work for each particle then becomes

$$W_i = \frac{8}{15} \frac{\bar{Y}_i}{1-\nu_i^2} \sqrt{\frac{R_i}{2}} \tilde{\delta}_{n,max,i}^{\frac{5}{2}}, \tag{8}$$

where $i \in \{A, S\}$. By substituting the work terms in Eq. (7) and the repelling forces in both particles being equal for maximum compression, the expression for the composite coefficient of restitution between Al_2O_3 and $SrFeO_{3-\delta}$ results in:

$$e_{AS}^2 = \frac{e_A^2 \left(\frac{\bar{Y}_S}{1-\nu_S^2} \sqrt{R_S} \right)^{\frac{2}{3}} + e_S^2 \left(\frac{\bar{Y}_A}{1-\nu_A^2} \sqrt{R_A} \right)^{\frac{2}{3}}}{\left(\frac{\bar{Y}_A}{1-\nu_A^2} \sqrt{R_A} \right)^{\frac{2}{3}} + \left(\frac{\bar{Y}_S}{1-\nu_S^2} \sqrt{R_S} \right)^{\frac{2}{3}}} \tag{9}$$

Using the fact that the Young's moduli $\bar{Y}_A$ and $\bar{Y}_S$ are both set to the minimum allowed value in LIGGGHTS®, and $\nu_A = \nu_S$ (compare

Table 2
Resulting contact parameters used for the high temperature DEM simulation of the PMR experimental setup. Corresponding calibration simulations were conducted using $\bar{Y} = 5\,\mathrm{MPa}$ and $\nu = 0.3$ for all materials.

Material combination		Friction coefficient	Rolling friction coefficient	Coefficient of restitution
Contact partner 1	Contact partner 2	μ	μ_r	e
$SrFeO_{3-\delta}$ particles	$SrFeO_{3-\delta}$ particles	0.28	0.38	0.24
Al_2O_3 particles	Al_2O_3 particles	0.31	0.10	0.75
$SrFeO_{3-\delta}$ particles	Coated wall	0.39	0.14[a]	0.48
Al_2O_3 particles	Coated wall	0.36	0.14	0.50
Al_2O_3 particles	$SrFeO_{3-\delta}$ particles	0.30	0.13	0.53[b]

[a] The $SrFeO_{3-\delta}$ rolling friction coefficient $\mu_{r,Sw}$ was interpolated due to non-intersecting contour lines.
[b] The composite coefficient of restitution e_{AS} was calculated from Eq. (10).

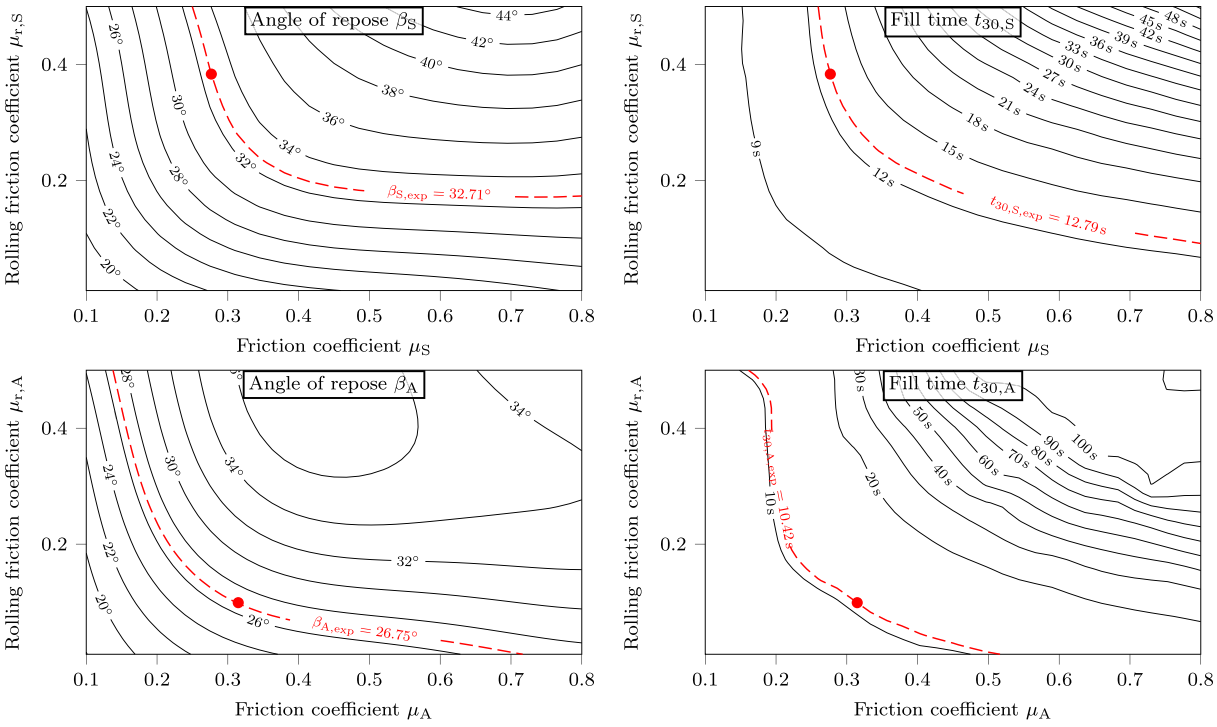

Fig. 8. Calibration simulation results for stage 1: Angles of repose and fill times from horizontal conveyor experiment with adhered particles, for $SrFeO_{3-\delta}$ (top) and Al_2O_3 particles (bottom). Experimental levels given as red dashed contours.

Section 2.3.1), Eq. (9) simplifies to

$$e_{AS}^2 = \frac{e_A^2 R_S^{\frac{1}{3}} + e_S^2 R_A^{\frac{1}{3}}}{R_A^{\frac{1}{3}} + R_S^{\frac{1}{3}}}. \tag{10}$$

The result is included in Table 2.

3.3. Calibration results

The conducted calibration experimental runs are summarized in Table A.3. Total used particle sample masses differ depending on the sizes of particles, base plates and bins. The results are mean values obtained from runs that were replicated up to 10 times to keep the relative standard error of the mean to a level of about 1%. The figures for masses in the more distant bins in the impact plate test, mostly m_3, do not satisfy this target, which is noncritical to the method's validity as will be seen in the discussion of corresponding results further below.

The calibration simulation results, their connection to lab results and the determination of resulting contact parameters are presented using contour graphs in the following. For the first calibration stage, these are given in Fig. 8. Interpolation functions of simulated values are shown over ranges of the varied particle-particle input parameters, friction coefficient μ_{pp} and rolling friction coefficient $\mu_{r,pp}$, respectively. As anticipated, the angle of repose β increases with both μ_{pp} and $\mu_{r,pp}$ regardless the particle type. The higher μ_{pp}, the more pronounced is the effect of $\mu_{r,pp}$ — and vice versa. In the horizontal conveyor test, the fill time t_{30} rises virtually monotonic over μ_{pp} and $\mu_{r,pp}$ for both particle types. Again, the increase of t_{30} over one coefficient is stronger at higher levels of the other.

The experimental result levels are marked by red dashed contours in the graphs. For a pair of contact parameters to be valid, they must yield results in both test simulations that align with the experimental results. This occurs at the intersections of the result-level contours in the combined, i. e., superposed contour graphs. The intersections are marked by a red dot in the figures. For both $SrFeO_{3-\delta}$ and Al_2O_3 particles, there are unambiguous intersections found yielding the particle-particle friction and rolling friction coefficients. Numerical values are found in Table 2. While the friction coefficients are similar for both particle types, the rolling friction coefficient of Al_2O_3 particles is significantly lower. This may be attributed to their smoother surface and larger diameter.

Fig. 9 pictures interpolated simulation results for stage 2, that is, angle of repose and horizontal conveyor test on plates of bare wall material without adhered particle layers. The angle of repose reaches an approximate plateau at values $\mu_{Sw} \gtrsim 0.25$ and $\mu_{r,Sw} \gtrsim 0.15$ for

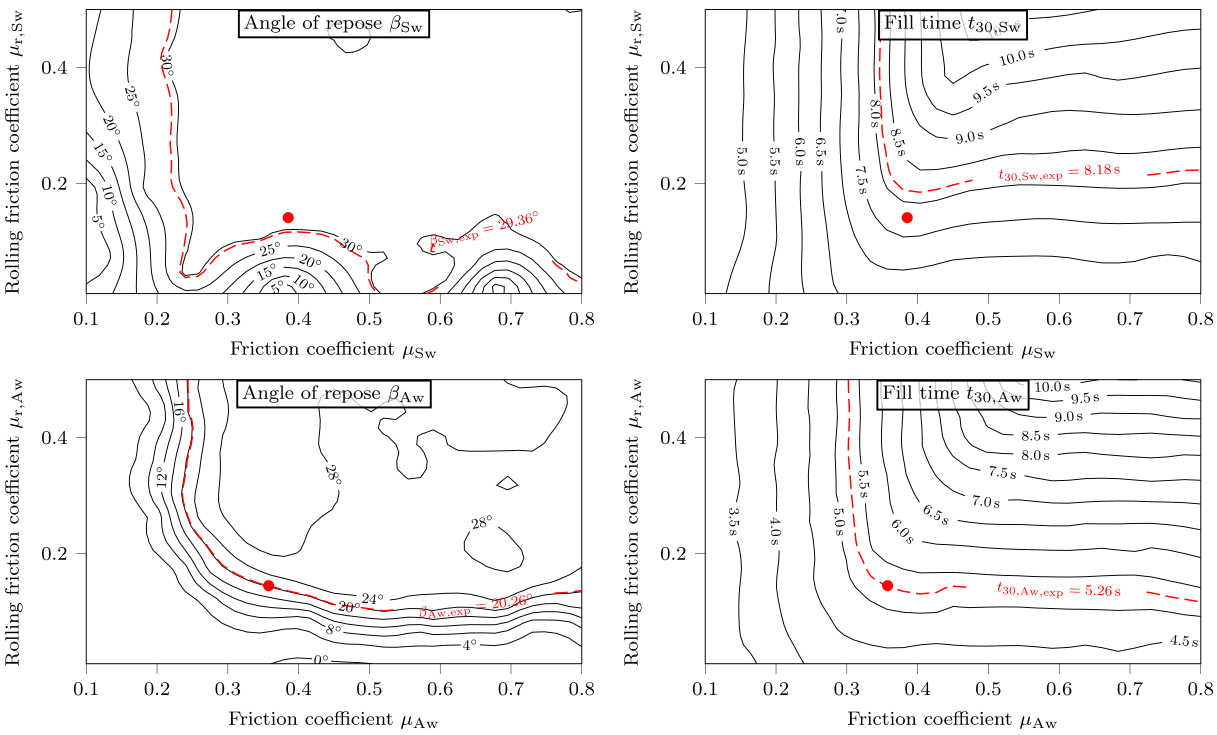

Fig. 9. Calibration simulation results for stage 2: Angles of repose and fill times from horizontal conveyor experiment on coated wall material, for $SrFeO_{3-\delta}$ (top) and Al_2O_3 particles (bottom). Experimental levels given as red dashed contours.

$SrFeO_{3-\delta}$ as well as $\mu_{Aw} \gtrsim 0.3$ and $\mu_{r,Aw} \gtrsim 0.15$ for Al_2O_3 particles. The levels of these plateaus are determined by particle-particle friction and thus close to the experimental values from above runs with adhered particles, i. e., infinite particle-wall friction forces. The same applies in the horizontal conveyor case: the fill times t_{30} measured in the experiments in stage 1 are not exceeded in the simulations of stage 2. The corresponding graphs illustrate a similar behavior for both particle types. At low coefficients of friction ($\mu_{pw} \lesssim 0.3$), t_{30} is almost independent of rolling friction. For higher μ_{pw}, there is a clear increase of t_{30} over $\mu_{r,pw}$, while the maximum attained value still rises with μ_{pw}.

For $\mu_{r,Sw} < 0.1$ the angle of repose characteristics of $SrFeO_{3-\delta}$ particles are somewhat erratic and rather seem to be caused by interpolation. It is not plausible for β to vary between 5° and 25° when increasing μ_{Sw} from 0.2 to 0.8. There was further no intersection found for the two result level contours of $SrFeO_{3-\delta}$ particles, so these contact parameters were interpolated on the closest path between the contours. Refining the sampling grid, which might have cleared up the irregularities, however, was omitted due to time constraints. While no parameter combination can satisfy both experimental results, the deviation to $\beta_{Sw,exp}$ is below 2° (7%) and to $t_{30,Sw,exp}$ is below 0.5 s (6%) for the interpolated parameter set. Therefore, this parameter combination is considered sufficiently accurate to represent the particles. For Al_2O_3 in contrast, two intersections were found (at $\mu_{Aw} = 0.36$ and $\mu_{Aw} = 0.74$). The plate surface, a densely sintered alumina coating, is of similar texture as Al_2O_3 particles. Therefore the lower value, which better matches μ_A of Al_2O_3 particles determined in stage 1, was selected.

The impact plate results (stage 3) are found in Fig. 10. As particle-wall and particle-particle restitution coefficients decrease, so does the mean post-collision particle momentum pointing away from the plate. This results in higher masses in bin 1 for both particle types. In case of $SrFeO_{3-\delta}$, the mass $m_{2,S}$ in bin 2 is surprisingly more strongly dependent on e_S than on e_{Sw}, probably due to a higher number of particle-particle collisions. This is in contrast to $m_{2,A}$, which is virtually independent of e_A.

There are two intersections found for Al_2O_3 in the superposition of the $m_{1,A}$ and $m_{2,A}$ graphs — on both flanks of the maximum for $m_{2,A}$. Choosing the upper one, i. e., at $e_{Aw} = 0.5$, is justified by findings for $m_{3,A}$: The experimental result $m_{3,A,exp}$ is reached at $e_{Aw} = 0.53$ and $e_{Aw} = 0.67$, almost independently of e_A. The conformity of simulated and experimental results for masses in the three bins is satisfied in this way. Thus, despite its fairly high standard error of the mean, m_3 serves to resolve the ambiguity. For $SrFeO_{3-\delta}$ there is a single intersection yielding a distinct pair of e_S and e_{Sw}.

The final fourth calibration stage again uses contour graphs for angle of repose and horizontal conveyor simulations of Al_2O_3 particles on adhered $SrFeO_{3-\delta}$ particles as shown in Fig. 11. Their shapes are similar to those in Fig. 8 with lower maximum levels of β and t_{30} due to the finer $SrFeO_{3-\delta}$ particles forming a smoother surface than adhered Al_2O_3 particles. With $\mu_{AS} = 0.3$ and $\mu_{r,AS} = 0.13$, all required contact parameters are determined.

4. Results and discussion

4.1. Particle motion

A qualitative result is presented in terms of particle motion during the mixing process at ambient temperature in Fig. 12. Pictures of the mixer being equipped with a transparent cover were recorded using a high-speed camera. They are compared to corresponding scenes from the simulation. Falling particles show similar cone shapes and traveled distances and no considerable deviation in terms of particle motion can be observed. This supports the applied model assumptions and simplifications, especially the neglected gas phase. A more distinct segregation between particle types on the ramp, however, appears to be present in the experiment. The denser $SrFeO_{3-\delta}$ particle cloud in the experiment is attributed to the generation of fines and dust of lower sinking velocity. Resulting discrepancies in mixture homogeneity of the bed are quantified in the following section.

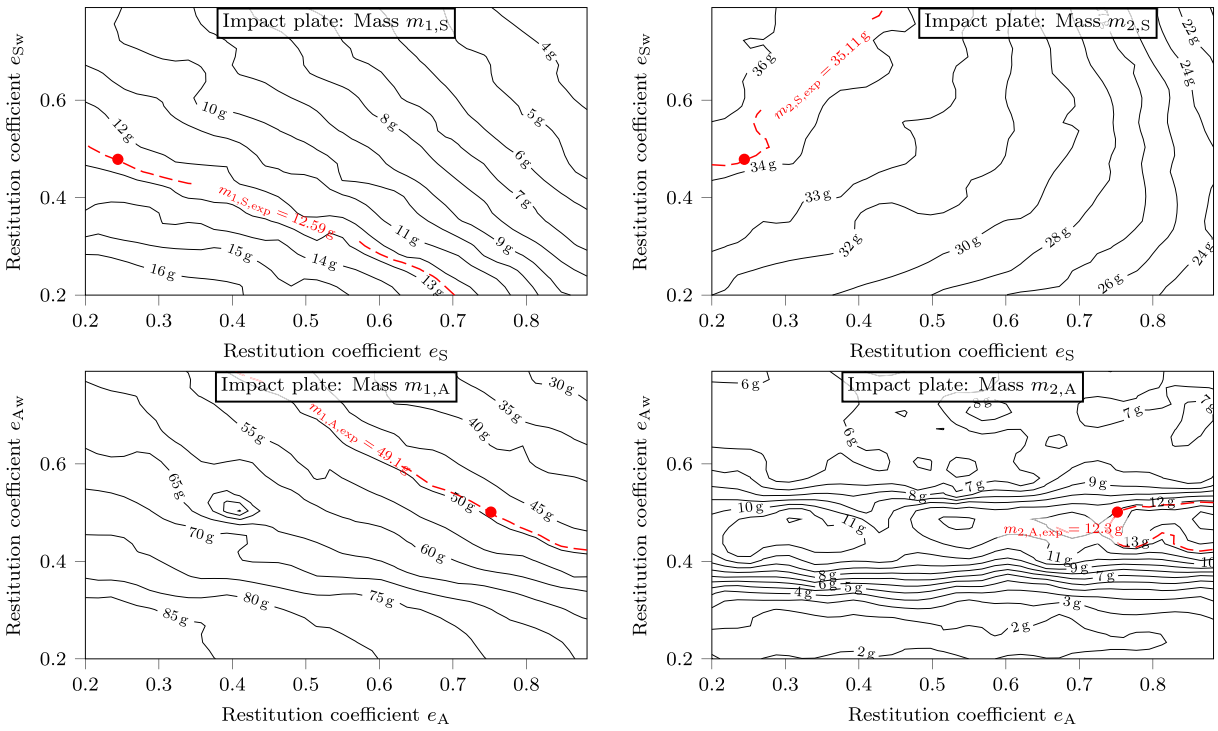

Fig. 10. Calibration simulation results for stage 3: Masses in bins 1 and 2 from impact plate test, for $SrFeO_{3-\delta}$ (top) and Al_2O_3 particles (bottom). Experimental levels given as red dashed contours.

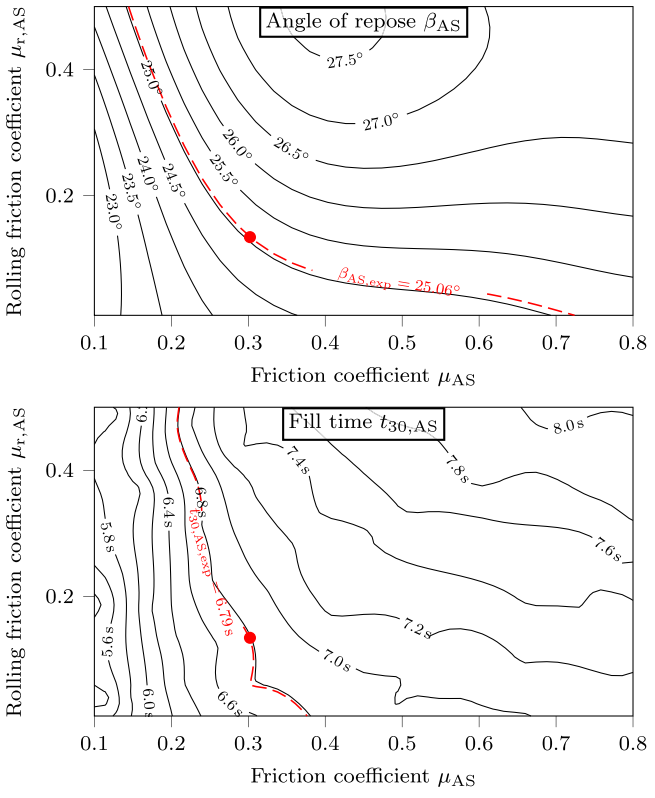

Fig. 11. Calibration simulation results for stage 4: Angle of repose and fill time from horizontal conveyor test of Al_2O_3 particles on adhered $SrFeO_{3-\delta}$ particles. Experimental levels given as red dashed contours.

4.2. Mixture homogeneity

The influence of mixture homogeneity on heat transfer in the reactor has been pointed out in Section 1, and the procedure of its measurement and evaluation was described in Section 2.2.2. It is thus a performance metric and relevant for interpretation of temperature developments. In addition, as the determination of DEM contact parameters in Section 3 employed particles at ambient temperatures, a possible effect on mixture homogeneity through temperature dependency of these parameters was examined. Analyses were therefore carried out on different mixtures produced from particles at both ambient and high temperatures (700 °C/1100 °C) at an opening delay of 125 ms.

4.2.1. Experimental results for varied temperatures

Fig. 13 displays the results in terms of the mass ratio $w = \frac{m_A}{m_S}$ between Al_2O_3 (subscript A) and $SrFeO_{3-\delta}$ particles (subscript S). The upper part of the figure differentiates per layer, i. e., height, and azimuth angle of the section centerline, the lower part shows mean mass ratios $\bar{w}$ per layer.

Evaluated mass ratios deviate considerably from an ideal homogeneity of $w = 1$ in both circumferential and axial direction. The circumferential distribution shows a characteristic peak in the half cylinder on the far side of the mixer ramp ($90° < \varphi < 270°$) for all layers except Layer 1. In Layers 2 to 4, the maximum value is reached at $\varphi = 180°$, while in the lower layers, especially Layer 5, some runs exhibit local minima at this position. There is a noticeable deviation from symmetry about $\varphi = 180°$, that is, the xz symmetry plane of the experimental setup: except for Layer 1, relatively higher mass ratios are found in the region $180° < \varphi < 360°$. Looking at mean mass ratio curves (averaged over the replicated runs) for a potential temperature dependency, the peaks around $\varphi = 180°$ in Layers 2 to 5 are lower for ambient temperature, while the valleys on the opposite side ($315° \leq \varphi \leq 45°$) are higher. These deviations, however, are of similar extent as those between individual replicated runs conducted at the same temperature. Layers 1 and 6 do not show a distinct influence

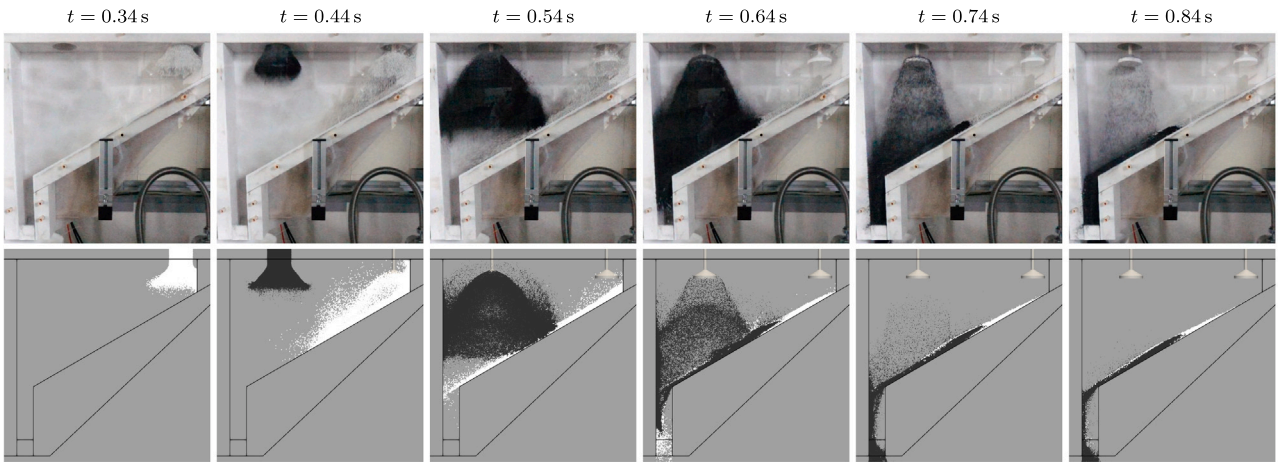

Fig. 12. The mixing process in showcase experiment and simulation over time after particle valve release, at an actual opening delay of 100 ms. Recognizing Al_2O_3 particles in the experiment is difficult due to low background contrast.

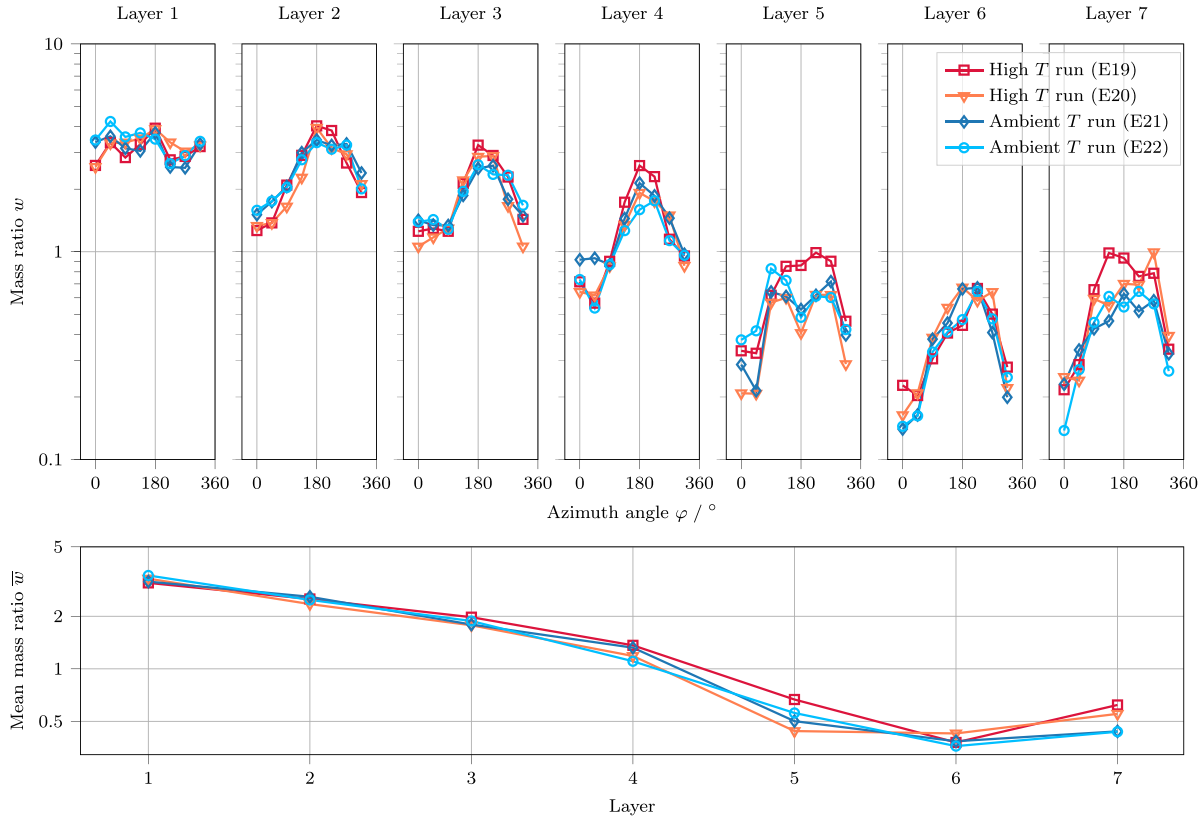

Fig. 13. Experimental mixture homogeneity results for runs at high temperature ($T_{0,A}$ = 1100 °C, $T_{0,S}$ = 700 °C) and at ambient temperature. Circumferential distributions per layer are indicated in the upper part, the axial distribution of mean layer values in the lower one. Refer to Fig. 6 for the definition of azimuth angle and layers.

of temperature and, as does Layer 7, mostly higher deviations between replications than between temperature levels. An altered homogeneity is moreover not necessarily due to a change of mechanical contact parameters and might be affected by thermal expansion of setup components and changes in their alignment. An effect of temperature on mixture homogeneity is thus not evident from this limited set of measurements. A more in-depth investigation would require additional data from dedicated experiments that exclude the above mentioned disturbances and is beyond the scope of this study.

Regarding mean values per layer in axial direction, there is a substantial excess of Al_2O_3 particles in the upper half of the bed, and consequentially vice versa for the lower half. Relative variations between the runs increase towards lower positions in the bed. There is no apparent effect of temperature.

4.2.2. Comparison of experimental and simulated results

As experimental runs with the IDs E21 and E22 were conducted at ambient temperature like the contact parameter calibration experiments, their averaged results were used for comparison to the DEM simulations, see Fig. 14. The simulated circumferential distributions of w within Layers 2 to 5 are in qualitative accordance with those from the experiment. At φ = 180°, respectively, they reflect the peaks in Layers 2 to 4 and the local minimum in Layer 5, though sharper and by exhibiting relative deviations of up to 60%. Discrepancies are

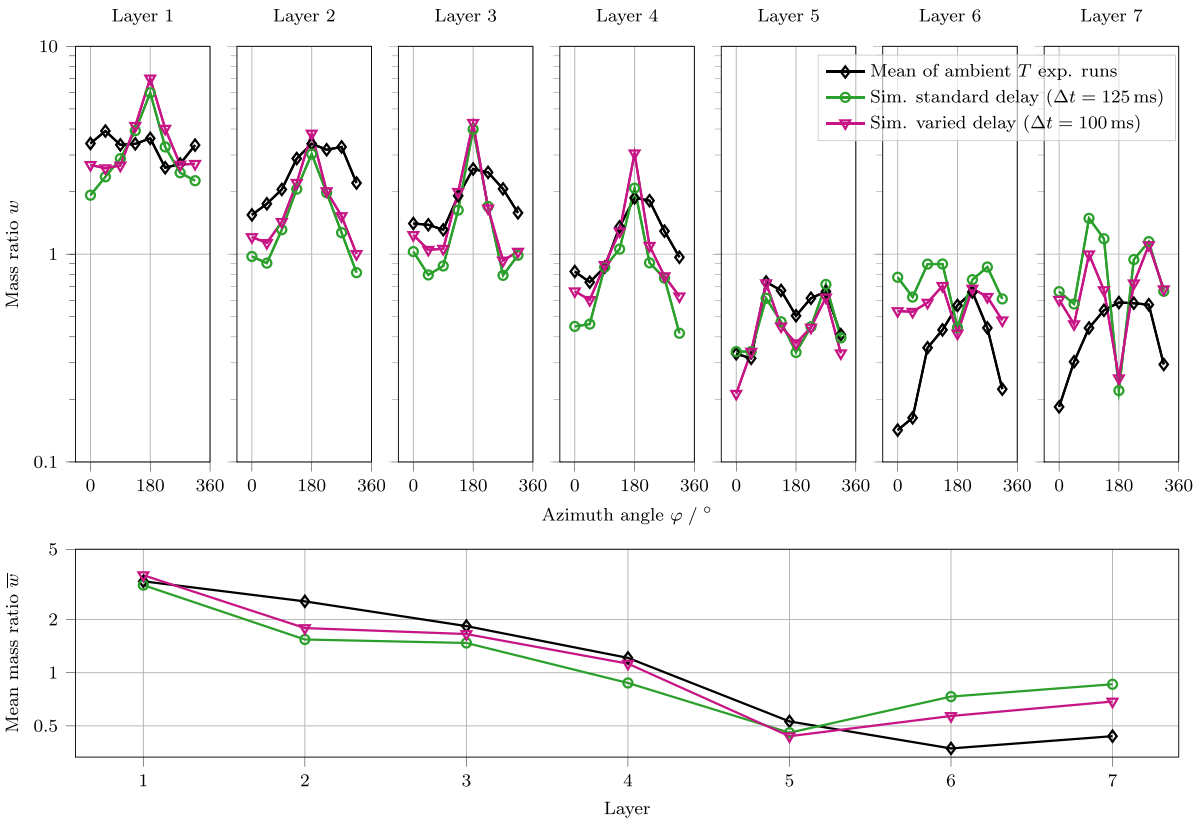

Fig. 14. Mixture homogeneity results from simulations at varied particle valve opening delay, compared to ambient temperature experimental mean.

most prominent in Layer 1, where the simulation yields a clear peak as opposed to the experiment. A detailed analysis of this discrepancy is beyond the scope of this study. It could arise from a neglected real-world property of the setup in the simulation (discussed below), as experiments are reproducible and the valve opening delay does not produce comparable deviations. Further, in Layers 6 and 7, vast relative deviations are found — as well as minima where none are present in the measurements. Symmetry is more pronounced in the simulation graphs. Still, between opposite sections equidistant to the xz plane, significant deviations of up to 30% are observed for an opening delay of 125 ms.

The axial decline of $\overline{w}$ towards lower layers in the experiment is represented qualitatively, though at a mean relative deviation of $\overline{\Delta w} = \frac{1}{7}\sum_{i=1}^{7}\left|1 - \frac{\overline{w}_{i,\mathrm{sim}}}{\overline{w}_{i,\mathrm{exp}}}\right| = 43\%$ for a delay of 125 ms, with especially high values in Layers 6 and 7. Analyses of high-speed camera recordings showed that with the opening delay set to 125 ms, actual delays between particle valve heads passing through the mixer inlet openings are between 100 and 130 ms. These analyses were conducted separately from the mixture homogeneity experiments shown here, and measurements of exact delays for each run (E19 to E22) could not be taken. To account for the expected uncertainty and to examine the impact on mixture homogeneity, a varied delay between particle valve releases of 100 ms was simulated in addition to the value of 125 ms. The two different delay values used in the simulation thus represent the setpoint case and a lower bound for the actual delay present in the experiment. Decreasing the opening delay to 100 ms in the simulation causes sensible changes in the axial distribution, in fact an increase of $\overline{w}$ in the upper layers and a decrease in the lower ones. This arises from an earlier insertion of $SrFeO_{3-\delta}$ particles into the mixer (compared to a delay of 125 ms) and their consequential accumulation in lower layers. The mean relative deviation to the experiment drops to 26%.

Potential contributions to measurement uncertainty are from an incomplete retention of a particle layer in the tool, displacement of particles and moderate agitation of the bed through sampling, presumably leading to its modification especially in lower layers. Higher relative deviations between runs in Layers 6 and 7 might indicate this. Simulation inputs and experimental conditions add further uncertainty: DEM contact parameters, the actual geometry of the setup holding deviations in alignment and orientation of components, surface irregularities and oscillation of the setup. Some aspects are neglected in the model in the first place, such as particle shape, particle size distribution and the presence of a gas phase, all of them affecting particle motion.

Despite this variety of uncertainties, the main inhomogeneity in the experiments – excess of Al_2O_3 particles in upper layers as well as on the far side of the mixer ramp – satisfactorily matched the simulations. The relative deviation figures are high. It should be considered, however, that the mass ratio w is very sensitive to particle concentration, as the numerator increases with a decreasing denominator. Using the mass ratio thus yields higher quantitative deviations compared to using the concentration.

Both measurements and simulation reveal a relevant improvement potential for mixture homogeneity in a scaled-up reactor to enhance heat transfer and minimize heat losses. The introduction of additional installations in the flow path could be examined in dedicated simulation campaigns using the here presented DEM model, that allows to simulate particle mixtures at reasonable accuracy.

5. Conclusion

The different particle states in terms of spatially resolved bed porosity occurring in the PMR experimental setup are effectively simulated by DEM. In addition, the particle-scale resolution of the DEM holds

major advantages regarding heat transfer modeling that is crucial to assess reactor performance in the indirect redox concept.

The mechanical contact parameters are necessary inputs for the simulation model. They were determined through a calibration approach using three different lab experiments and their simulated equivalents, which was first applied to uniform particles. As $SrFeO_{3-\delta}$ particles in combination with Al_2O_3 particles were used in the setup, the calibration procedure was extended to also consider interactions between different particle types. For contacts between similar particles, unambiguous pairs of friction and rolling friction coefficients are found for both particle types. The coarser and smoother Al_2O_3 particles show lower rolling friction coefficients compared to $SrFeO_{3-\delta}$ particles. Simulated angles of repose for $SrFeO_{3-\delta}$ are oscillating over μ_{Sw} in the range $\mu_{r,Sw} < 0.1$ and the resulting pair of μ_{Sw} and $\mu_{r,Sw}$ is interpolated. A different behavior of the particle types is observed in stage 3 using the impact plate experiment. Masses of $SrFeO_{3-\delta}$ particles in bin 2 are far more sensitive to the particle-particle restitution coefficient than Al_2O_3 particles due to a higher number of collisions. A distinct pair of e_S and e_{Sw} is found, while for Al_2O_3, the result for bin 3 had to be taken into account for accuracy. In the appended fourth calibration stage, friction and rolling friction coefficient between $SrFeO_{3-\delta}$ and Al_2O_3 particles are identified. Their composite coefficient of restitution is derived analytically.

The comparison of particle motion during mixing for both experiment and simulation revealed largely similar trajectories, apart from generated fines that remain disregarded in the simulation. The distributions of mixture homogeneity in the settled bed, which are ultimately relevant to interpreting temperature results, were measured by a novel tool for non-destructive segmentation. Between experiment and simulation, although at considerable quantitative deviations, we found qualitatively similar distributions. The mean relative deviation between layer-averaged values is 26% at a valve opening delay of 100 ms in the simulation. This agreement is satisfactory given the sensitivity of the evaluated mass ratio w and indicates a valid representation of particle mechanics.

The results show a distinct improvement potential of the mixture quality in circumferential and axial direction. An excess of Al_2O_3 particles in upper bed layers and on the far side of the ramp is observed. A temperature influence on mixture homogeneity cannot be concluded, as effects were small with respect to repeated testing and, where present, might as well be caused by geometrical changes of the setup through thermal expansion. In view of thermal reactor performance, the obtained homogeneity distributions are reflected in measured and simulated particle temperature distributions that will be addressed in a forthcoming publication.

CRediT authorship contribution statement

Sebastian Richter: Writing – original draft, Visualization, Validation, Software, Methodology, Investigation, Formal analysis, Data curation, Conceptualization. **Johannes Grobbel:** Writing – review & editing, Validation, Software, Methodology, Investigation. **Stefan Brendelberger:** Writing – review & editing, Supervision, Methodology, Conceptualization. **Martin Roeb:** Writing – review & editing, Supervision, Funding acquisition. **Christian Sattler:** Writing – review & editing, Supervision, Funding acquisition.

Declaration of competing interest

The authors declare that they have no known competing financial interests or personal relationships that could have appeared to influence the work reported in this paper.

Acknowledgments

The work has received funding from the Helmholtz Association within the virtual institute SolarSynGas (VH-VI-509) and German Aero space Center (DLR) base funding within the project Future Fuels 2.

Appendix A

A.1. DEM model equations

A.1.1. Spring stiffness and damping coefficient models

The normal spring stiffness required in Eq. (3) is given as

$$\tilde{k}_n = \frac{4}{3}\bar{Y}_{red}\sqrt{R_{red}\tilde{\delta}_n}\,, \tag{A.1}$$

with the reduced radius

$$R_{red} = \frac{R_i R_j}{R_i + R_j}\,, \tag{A.2}$$

and the radii R_i and R_j of the two contacting particles. The reduced Young's modulus is obtained from

$$\frac{1}{\bar{Y}_{red}} = \frac{1-\nu_i^2}{\bar{Y}_i} + \frac{1-\nu_j^2}{\bar{Y}_j}\,, \tag{A.3}$$

where ν and $\bar{Y}$ represent the Poisson's ratio and the Young's modulus of the respective particle (subscripts i, j), respectively.

The damping coefficient, again a function of the normal overlap, is determined as follows [31]:

$$c_n = -\frac{2\ln(e)}{\sqrt{\ln^2(e)+\pi^2}}\sqrt{\frac{5}{3}m_{red}\bar{Y}_{red}\sqrt{R_{red}\tilde{\delta}_n}} \tag{A.4}$$

Here, e is the coefficient of restitution, i. e., the ratio of the relative velocity of the particles past collision to the initial relative velocity. The reduced mass m_{red} is given as

$$\frac{1}{m_{red}} = \frac{1}{m_i} + \frac{1}{m_j}\,. \tag{A.5}$$

The tangential displacement $\tilde{\delta}_t$ from Eq. (4) is less intuitive than $\tilde{\delta}_n$ in normal direction. According to the LIGGGHTS 3.8.0 source code for the tangential history model, the new displacement vector $\vec{\delta}_t^{new}$ in the tangential direction on the contact plane with normal vector $\vec{e}_n$ is calculated by Eq. (A.6). The tangential displacement $\tilde{\delta}_t$ is its Euclidian norm.

$$\vec{\delta}_t^{new} = \vec{\delta}_t^{old} + \vec{v}_{t,rel}\Delta t - \left(\left(\vec{\delta}_t^{old} + \vec{v}_{t,rel}\Delta t\right)\cdot\vec{e}_n\right)\cdot\vec{e}_n \tag{A.6}$$

The relative tangential velocity $\vec{v}_{t,rel}$ results from the relative velocity of the particle centers and from the angular velocities of the particles. Its Euclidian norm is used in Eq. (4). As the old displacement vector is not necessarily in the new contact plane, a projection into the plane is made in Eq. (A.6).

When sliding occurs, the maximum tangential force is limited to the Coulomb friction force (see Eq. (5)) and the displacement vector is calculated by equation Eq. (A.7).

$$\vec{\delta}_t^{new} = \frac{\vec{F}_{c\to i,t}}{\tilde{k}_t} \tag{A.7}$$

The tangential spring stiffness [32]

$$\tilde{k}_t = 8\bar{G}_{red}\sqrt{R_{red}\tilde{\delta}_n} \tag{A.8}$$

and the tangential damping coefficient

$$c_t = -\frac{2\ln(e)}{\sqrt{\ln^2(e)+\pi^2}}\sqrt{\frac{5}{6}m_{red}\tilde{k}_t} \tag{A.9}$$

are again given as (direct or indirect) functions of the normal overlap. The reduced shear modulus $\bar{G}_{red}$ is obtained from the individual Young's moduli by

$$\frac{1}{\bar{G}_{red}} = \frac{2(2-\nu_i)(1+\nu_i)}{\bar{Y}_i} + \frac{2(2-\nu_j)(1+\nu_j)}{\bar{Y}_j}\,. \tag{A.10}$$

Table A.3
Specifications and results for calibration experiments to obtain contact parameters for the DEM model. To limit the testing workload, the number of runs was adjusted to achieve a relative standard error (RSE) of the mean of approximately 1%, compare Section 3.3.

Particle type	Fixed base	Stage	Particle mass/g	Runs	Mean result	RSE of the mean/%
Angle of repose test						
$SrFeO_{3-\delta}$	$SrFeO_{3-\delta}$ particles	1	150	10	$\beta_{S,exp} = 32.7°$	0.6
Al_2O_3	Al_2O_3 particles	1	400	10	$\beta_{A,exp} = 26.8°$	0.8
$SrFeO_{3-\delta}$	Coated wall	2	150	10	$\beta_{Sw,exp} = 29.4°$	1.2
Al_2O_3	Coated wall	2	400	10	$\beta_{Aw,exp} = 20.3°$	1.2
Al_2O_3	$SrFeO_{3-\delta}$ particles	4	400	10	$\beta_{AS,exp} = 25.1°$	0.9
Horizontal conveyor test						
$SrFeO_{3-\delta}$	$SrFeO_{3-\delta}$ particles	1	120	3	$t_{30,S,exp} = 12.8\,s$	0.1
Al_2O_3	Al_2O_3 particles	1	120	3	$t_{30,A,exp} = 10.4\,s$	0.3
$SrFeO_{3-\delta}$	Coated wall	2	120	3	$t_{30,Sw,exp} = 8.18\,s$	1.0
Al_2O_3	Coated wall	2	120	3	$t_{30,Aw,exp} = 5.26\,s$	0.2
Al_2O_3	$SrFeO_{3-\delta}$ particles	4	120	3	$t_{30,AS,exp} = 6.79\,s$	1.4
Impact plate test						
$SrFeO_{3-\delta}$	Coated wall	3	100	5	$m_{1,S,exp} = 12.6\,g$	0.7
					$m_{2,S,exp} = 35.1\,g$	0.4
					$m_{3,S,exp} = 1.30\,g$	6.0
Al_2O_3	Coated wall	3	100	10	$m_{1,A,exp} = 49.1\,g$	1.2
					$m_{2,A,exp} = 12.3\,g$	2.6
					$m_{3,A,exp} = 2.71\,g$	6.9

Table A.4
Masses in sections and adjusted layer thicknesses.

Layer	Mass per layer in g						Layer thickness
	E19	E20	E21	E22	Exp. mean	Simulation	in cm
1	235.47	259.06	258.32	283.49	259.09	259.35	1.965
2	265.78	257.54	279.39	264.36	266.77	266.76	1.515
3	248.15	270.98	283.06	281.39	270.89	270.74	1.567
4	260.52	316.56	307.89	284.22	292.3	292.4	1.718
5	260.68	278.6	252.73	272.08	266.02	266.11	1.566
6	269.22	255.98	255.21	257.65	259.52	259.47	1.497
7	208.22	170.68	200.59	170.19	187.42	187.54	1.095
Residuum	250.93	205.33	154.38	177.45	197.02	197.05	1.175

A.1.2. Rolling friction

The EPSD2 model consists of an elastic rolling friction torque component,

$$\frac{\mathrm{d}\vec{M}_{\mathrm{rf}}}{\mathrm{d}t} = -\tilde{k}_{\mathrm{t}} R_{\mathrm{red}}^2 \frac{\mathrm{d}\varphi_{\mathrm{rel}}}{\mathrm{d}t}, \tag{A.11}$$

with the relative rotation of the two particles φ_{rel}.

A.2. Calibration experiment results

The detailed results of the calibration experiments are shown in Table A.3.

A.3. Mixture analysis results

The results of the mixture analysis are displayed in Table A.4.

References

[1] IPCC, Climate change 2023: Synthesis report: A report of the intergovernmental panel on climate change. Contribution of working groups i, II and III to the sixth assessment report of the intergovernmental panel on climate change, 2023.

[2] M. Ram, T. Galimova, D. Bogdanov, M. Fasihi, A. Gulagi, C. Breyer, M. Micheli, K. Crone, Powerfuels in a renewable energy world: Global volumes, costs, and trading 2030 to 2050, 2020.

[3] W.C. Chueh, C. Falter, M. Abbott, D. Scipio, P. Furler, S.M. Haile, A. Steinfeld, High-flux solar-driven thermochemical dissociation of CO2 and H2O using nonstoichiometric ceria, Science 330 (2010) 1797–1801, http://dx.doi.org/10.1126/science.1197834.

[4] J. Lapp, J.H. Davidson, W. Lipiński, Efficiency of two-step solar thermochemical non-stoichiometric redox cycles with heat recovery, Energy 37 (1) (2012) 591–600, http://dx.doi.org/10.1016/j.energy.2011.10.045.

[5] B. Bulfin, F. Call, M. Lange, O. Lübben, C. Sattler, R. Pitz-Paal, I.V. Shvets, Thermodynamics of CeO2 thermochemical fuel production, Energy & Fuels 29 (2) (2015) 1001–1009, http://dx.doi.org/10.1021/ef5019912.

[6] A. Haeussler, S. Abanades, A. Julbe, J. Jouannaux, B. Cartoixa, Solar thermochemical fuel production from H2O and CO2 splitting via two-step redox cycling of reticulated porous ceria structures integrated in a monolithic cavity-type reactor, Energy 201 (2020) 117649, http://dx.doi.org/10.1016/j.energy.2020.117649.

[7] S. Zoller, E. Koepf, D. Nizamian, M. Stephan, A. Patané, P. Haueter, M. Romero, J. González-Aguilar, D. Lieftink, E. de Wit, S. Brendelberger, A. Sizmann, A. Steinfeld, A solar tower fuel plant for the thermochemical production of kerosene from H2O and CO2, Joule 6 (7) (2022) 1606–1616, http://dx.doi.org/10.1016/j.joule.2022.06.012.

[8] R. Schäppi, D. Rutz, F. Dähler, A. Muroyama, P. Haueter, J. Lilliestam, A. Patt, P. Furler, A. Steinfeld, Drop-in fuels from sunlight and air, Nature 601 (7891) (2022) 63–68, http://dx.doi.org/10.1038/s41586-021-04174-y.

[9] J. Lapp, J.H. Davidson, W. Lipiński, Heat transfer analysis of a solid-solid heat recuperation system for solar-driven nonstoichiometric redox cycles, J. Sol. Energy Eng. 135 (3) (2013) 031004, http://dx.doi.org/10.1115/1.4023357.

[10] J. Lapp, W. Lipiński, Transient three-dimensional heat transfer model of a solar thermochemical reactor for H2O and CO2 splitting via nonstoichiometric ceria redox cycling, J. Sol. Energy Eng. 136 (3) (2014) 237, http://dx.doi.org/10.1115/1.4026465.

[11] J.E. Miller, A.H. McDaniel, M.D. Allendorf, Considerations in the design of materials for solar-driven fuel production using metal-oxide thermochemical cycles, Adv. Energy Mater. 4 (2) (2014) 1300469, http://dx.doi.org/10.1002/aenm.201300469.

[12] S. Brendelberger, C. Sattler, Concept analysis of an indirect particle-based redox process for solar-driven H2O/CO2 splitting, Sol. Energy 113 (2015) 158–170, http://dx.doi.org/10.1016/j.solener.2014.12.035.

[13] S. Richter, S. Brendelberger, F. Gersdorf, T. Oschmann, C. Sattler, Demonstration reactor system for the indirect solar-thermochemical reduction of redox particles—The particle mix reactor, J. Energy Resour. Technol. 142 (5) (2020) 249, http://dx.doi.org/10.1115/1.4046315.

[14] J. Grobbel, Modeling Solar Particle Receivers with the Discrete Element Method (Dissertation), RWTH Aachen, 2018, http://dx.doi.org/10.18154/RWTH-2020-01764.

[15] J. Grobbel, S. Brendelberger, M. Henninger, C. Sattler, R. Pitz-Paal, Calibration of parameters for DEM simulations of solar particle receivers by bulk experiments and surrogate functions, Powder Technol. 364 (2020) 831–844, http://dx.doi.org/10.1016/j.powtec.2019.11.028.

[16] J. Vieten, B. Bulfin, F. Call, M. Lange, M. Schmücker, A. Francke, M. Roeb, C. Sattler, Perovskite oxides for application in thermochemical air separation and oxygen storage, J. Mater. Chem. A 4 (35) (2016) 13652–13659, http://dx.doi.org/10.1039/C6TA04867F.
[17] C. Thornton, Granular Dynamics, Contact Mechanics and Particle System Simulations: A DEM Study, Vol. 24, Springer International Publishing, Cham, 2015, http://dx.doi.org/10.1007/978-3-319-18711-2.
[18] T. Pöschel, T. Schwager, Computational Granular Dynamics: Models and Algorithms, Springer, Berlin, 2005, http://dx.doi.org/10.1007/3-540-27720-X.
[19] T. Gröger, A. Katterfeld, On the numerical calibration of discrete element models for the simulation of bulk solids, 21, 2006, pp. 533–538, http://dx.doi.org/10.1016/s1570-7946(06)80100-8.
[20] M. Marigo, E.H. Stitt, Discrete element method (DEM) for industrial applications: Comments on calibration and validation for the modelling of cylindrical pellets, KONA Powder Part. J. 32 (2015) 236–252, http://dx.doi.org/10.14356/kona.2015016.
[21] C. O'Sullivan, Particulate Discrete Element Modelling: A Geomechanics Perspective, first ed., in: Applied Geotechnics, vol. 1, Taylor & Francis, Abingdon England, 2011.
[22] H. Kruggel-Emden, E. Simsek, S. Rickelt, S. Wirtz, V. Scherer, Review and extension of normal force models for the discrete element method, Powder Technol. 171 (3) (2007) 157–173, http://dx.doi.org/10.1016/j.powtec.2006.10.004.
[23] J. Ai, J.-F. Chen, J.M. Rotter, J.Y. Ooi, Assessment of rolling resistance models in discrete element simulations, Powder Technol. 206 (3) (2011) 269–282, http://dx.doi.org/10.1016/j.powtec.2010.09.030.
[24] V.L. Popov, Contact Mechanics and Friction: Physical Principles and Applications, Springer Berlin Heidelberg, 2017, http://dx.doi.org/10.1007/978-3-662-53081-8.
[25] Y. Tsuji, T. Tanaka, T. Ishida, Lagrangian numerical simulation of plug flow of cohesionless particles in a horizontal pipe, Powder Technol. 71 (3) (1992) 239–250, http://dx.doi.org/10.1016/0032-5910(92)88030-L.
[26] C. Kloss, C. Goniva, A. Hager, S. Amberger, S. Pirker, Models, algorithms and validation for opensource DEM and CFD-DEM, Prog. Comput. Fluid Dyn. an Int. J. 12 (2/3) (2012) 140, http://dx.doi.org/10.1504/PCFD.2012.047457.
[27] K. Iwashita, M. Oda, Rolling resistance at contacts in simulation of shear band development by DEM, J. Eng. Mech. 124 (3) (1998) 285–292, http://dx.doi.org/10.1061/(ASCE)0733-9399(1998)124:3(285).
[28] C.J. Coetzee, Review: Calibration of the discrete element method, Powder Technol. 310 (2017) 104–142, http://dx.doi.org/10.1016/j.powtec.2017.01.015.
[29] M. Rackl, K.J. Hanley, A methodical calibration procedure for discrete element models, Powder Technol. 307 (2017) 73–83, http://dx.doi.org/10.1016/j.powtec.2016.11.048.
[30] J. Coaplen, W.J. Stronge, B. Ravani, Work equivalent composite coefficient of restitution, Int. J. Impact Eng. 30 (6) (2004) 581–591, http://dx.doi.org/10.1016/j.ijimpeng.2003.10.038.
[31] D. Antypov, J.A. Elliott, On an analytical solution for the damped Hertzian spring, EPL (Eur. Lett.) 94 (5) (2011) 50004, http://dx.doi.org/10.1209/0295-5075/94/50004.
[32] R.D. Mindlin, Compliance of elastic bodies in contact, J. Appl. Mech. 16 (3) (1949) 259–268.